Relationship between frontal dust storms and transient eddy activity in the northern hemisphere of Mars as observed by Mars Global Surveyor

Huiqun Wang
Division of Geological and Planetary Sciences, California Institute of Technology, Pasadena, California, USA

Richard W. Zurek
Jet Propulsion Laboratory, California Institute of Technology, Pasadena, California, USA

Mark I. Richardson
Division of Geological and Planetary Sciences, California Institute of Technology, Pasadena, California, USA

Received 25 February 2005; revised 9 May 2005; accepted 19 May 2005; published 29 July 2005.

[1] We have compiled a catalog of frontal dust storms in the northern hemisphere using Mars Orbiter Camera daily global maps spanning ~2.3 Martian years of Mars Global Surveyor (MGS) observations (from 1999 to 2003). The most vigorous frontal storms that flush dust to the low latitudes occur in early-mid fall and mid-late winter, away from the northern winter solstice. While many streaks are observed in the polar hood during the winter solstice period, no frontal dust storms are observed in the vicinity of the north polar region. We have also analyzed simultaneous MGS Thermal Emission Spectrometer (TES) temperature data and found statistically significant negative temperature anomalies associated with frontal storms. In the lowest scale height of the atmosphere, the geographical and seasonal distributions of temperature standard deviations associated with transient variations agree well with the distributions of frontal storms. The correlation deteriorates with increasing altitude, suggesting that lower-level temperature waves are associated with the frontal dust storms. Specifically, eastward traveling m = 3 waves with periods of 2–3 sols appear to be closely related to the development of flushing frontal storms.

Citation: Wang, H., R. W. Zurek, and M. I. Richardson (2005), Relationship between frontal dust storms and transient eddy activity in the northern hemisphere of Mars as observed by Mars Global Surveyor, *J. Geophys. Res.*, *110*, E07005, doi:10.1029/2005JE002423.

1. Introduction and Background

1.1. Introduction

[2] Dust storms are a major feature of Martian meteorology. With the advent of global and nearly continuous imaging of Mars with the Mars Global Surveyor (MGS) Mars Orbiter Camera (MOC), it has become possible to differentiate between different types of dust storms and study their distributions in detail. Published studies to date include those of *Cantor et al.* [2001], who documented the spatial, temporal and size distributions of all dust storms observed in 1999; *Wang et al.* [2003], who examined southward moving regional dust storms of 1999; and *Strausberg et al.* [2005], who documented the 2001 global dust storm. In this paper, we have analyzed ~2.3 Martian years of data for the northern hemisphere, focusing on a subtype of dust storms (frontal dust storms) whose linear or curvilinear structure and movement resemble the classical cloudband structure of terrestrial wintertime storm fronts. Examples of such storms have been noted before from Hubble Space Telescope and MOC images [*James et al.*, 1999; *Cantor et al.*, 2001; *Wang et al.*, 2003]. *Briggs and Leovy* [1974] found evidence for front-like cloud features in northern winter midlatitudes using Mariner 9 images. In several instances, local dust storms appeared to be associated with the frontal systems.

[3] On the basis of their appearance, it has been assumed that frontal dust storms are the result of dust being raised from the surface by strong winds associated with the intensified pressure and temperature gradients in storm systems. The storm systems are probably generated by the baroclinic instability at the edge of the polar vortex. Dust is spread behind the moving front, helping to identify the larger storm system, but also being part of the air mass exported to lower latitudes.

[4] The existence of baroclinic weather systems on Mars is expected from the general theory of atmospheric circulations for Earth and Mars, which are rapidly rotating planets with thin atmospheres driven strongly by heat

0148-0227/05/2005JE002423$09.00

exchange with the surface and subject to large seasonal variations due to the tilt of their rotation axis [*Zurek et al.*, 1992]. Numerical simulations for Mars indicate the development of baroclinic systems consistent with visual observations of cloud and dust variations [*Briggs and Leovy*, 1974; *James et al.*, 1999; *Wang et al.*, 2003] and with the pressure, temperature and wind variations observed at the surface by Viking Lander 2 (48°N) [e.g., *Barnes et al.*, 1993; *Collins et al.*, 1996; *Wilson et al.*, 2002]. The simulated heat flux and momentum flux can be used to examine energy conversion. *Barnes et al.* [1993] showed that the simulated transient eddies generated the bulk of their energy baroclinically at both lower and upper levels and they generated a substantial amount of energy barotropically as well. *Wilson et al.* [2002] showed latitude-height structure of the observed and simulated traveling waves, and stated that they were consistent with baroclinic instability.

[5] The data available for this study take the form of Mars daily global maps derived from MGS MOC images and atmospheric temperature profiles derived from the MGS Thermal Emission Spectrometer (TES). The principal advantages of the MGS data sets are the systematic daily, global coverage for a period that spans more than two Martian years. Furthermore, the horizontal resolution and spatial coverage of the MOC wide-angle images reveal the frontal features and regional phenomena in which we are interested. However, TES data are limited to 12–13 orbital tracks per day and TES retrievals have limited vertical resolution (about half an atmospheric scale height). A hallmark of a baroclinically unstable wave would be a tilting of the vertical structure with height and longitude. As a result, it is difficult to resolve ''frontal'' structure with TES data. Nevertheless, MGS data provide the global view unavailable from previous observations to further test simulation results. The vertical structures of simulated baroclinic waves suggest that waves with zonal wave number 1 are deep and those with larger wave numbers tend to be localized near the surface [*Barnes et al.*, 1993; *Wilson et al.*, 2002]. With TES data, we can examine whether the visually observed frontal dust storms are associated with deep or shallow temperature perturbations, and this is a vital clue. Also, TES temperature data provide the best characterization of the seasonally varying ''background'' atmospheric structure in which the traveling waves are embedded.

[6] Here, we specifically focus on examining the correlation between frontal development observed in images and thermal perturbations at various levels in the atmosphere associated with traveling waves. At high latitudes one can think of the traveling waves as distortions of a more zonally symmetric latitudinal gradient of temperature, which can be represented mathematically as a series of waves (i.e., variations with longitude). This representation is particularly useful when examining the TES temperature data. It is still useful when describing the organized condensate and dust patterns seen in the visual observations of the polar regions, but once the storm (and its associated dust front) has moved away from the polar vortex, one is really dealing with a specific event and not a ''wave train'' at that particular latitude. In this paper, we ask whether there is any further observational evidence that the dust fronts are associated with baroclinic storm systems and, whether there are patterns in the timing and scale of the storm systems with dust fronts that can be related to the hemispheric temperature structure. In summary, the purposes of this paper are as follows:

[7] 1. Establish the seasonal variability of frontal dust storms based on MOC imagery, including the spatial scale and frequency of the storm systems in which they are embedded.

[8] 2. Use temperatures retrieved from TES orbital data to test the hypothesis that frontal dust storms are embedded in midlatitude baroclinic storm (traveling wave) systems.

[9] 3. Examine the relationship between the seasonal variability of the frontal storms, of the transient waves in the atmosphere (i.e., compare seasonal variability of MOC imagery and TES temperature variability), and of the structure of the polar vortex (based on TES temperatures and estimates of ''baroclinicity,'' the latter is based on theoretical guidance).

1.2. Overview of Past Work

[10] Since dust storms and clouds reflect the meteorological conditions under which they form and indicate atmospheric circulation patterns, they have been studied extensively. *French et al.* [1981] and *Kahn* [1984] documented the occurrence of different types of clouds using Mariner 9 and Viking images. *Cantor et al.* [2001] documented the occurrence of dust storms in 1999 using MGS MOC images. Previous classification of dust storms is mainly according to their sizes and positions, while this study classifies them according to their morphology and focuses on a particular type: a frontal dust storm that resembles a terrestrial baroclinic front. Some frontal storms develop into regional scale and transport dust from the north polar vortex edge southward to the low latitudes as they propagate eastward. These ''flushing'' storms generally occur in two seasonal windows L_s 200°–240° and L_s 300°–340° [*Cantor et al.*, 2001; *Wang et al.*, 2003]. This paper provides detailed description of the distribution of frontal dust storms including flushing storms. *Wang et al.* [2003] studied the mechanism of flushing storms with the Geophysical Fluid Dynamics Laboratory (GFDL) Mars General Circulation Model (GCM). Their results suggest that the synchronization between the low level winds in frontal systems and winds associated with the diurnal tide is key to the southward tracer transport. The seasonality of the simulated flushing storms is similar to that observed, though the simulation is under clear conditions year-round, which differs from the observed large increase of dust opacity in northern fall and winter. *Newman et al.* [2002] simulated a flushing storm in the Acidalia-Chryse channel using the Mars GCM developed at the Department of Atmospheric, Oceanic and Planetary Physics (AOPP) at the University of Oxford and the Laboratoire de Meteorologie Dynamique (LMD). In addition to MGS MOC, MGS TES and Mars Orbiter Laser Altimeter (MOLA) also provide simultaneous dust storm and cloud observations. *Smith* [2004] documented TES observations of dust and water ice optical depth. This is particularly useful for studying the evolution of background dust and regional/global scale dust storms and clouds. *Neumann et al.* [2003] documented two Mars years of clouds detected by the MOLA. Their results show

that absorptive clouds in the northern hemisphere minimizes around northern winter solstice.

[11] The literature contains quite extensive discussions of transient/baroclinic eddies in the Martian atmosphere. *Leovy and Mintz* [1969] generated fully nonlinear, primitive equation simulations of baroclinic waves. They found that the dominant zonal wave numbers of the transient eddies at equinox were m = 3 to 4, but m = 2 to 3 for solstice conditions. *Barnes* [1980, 1981] demonstrated that highly coherent pressure, wind and temperature perturbations observed by Viking Lander 2 (VL2, 48°N, 226°W) were consistent with eastward traveling baroclinic waves, centered to the north of the lander. In the first Viking year, greatly reduced transient eddy activity immediately followed the onset of the 1977b global dust storm which originated around the northern winter solstice [*Barnes*, 1980]. In the second Viking year which did not have any global or large regional dust storms, transient variation of zonal wind u' showed a reduction in wave amplitude during L_s 250°–305°, though the reduction was not as dramatic as that in the first Viking year and the reduction of eddy activity during this period was not obvious in transient pressure perturbation p' and meridional wind perturbation v' [*Barnes*, 1981]. All modes of eddies did not vanish throughout the northern fall and winter season, but the periods with reduced wave amplitudes were dominated with 6–8 sol eddies instead of shorter period (2–4 sol) eddies [*Barnes*, 1980, 1981]. *Barnes* [1984] studied linear baroclinic instability for the Martian atmosphere. He found that zonal wave numbers 3 and 4 were the most unstable in the midlatitudes, and that the growth rate was substantially decreased under enhanced static stability (such as resulting from increased dust opacity during dust storms). *Barnes et al.* [1993] further studied transient baroclinic waves generated by the NASA AMES GCM. They found strong transient baroclinic eddies characterized by zonal wave number of 1–4 and periods of 2–10 days in the extratropics of the northern hemisphere during northern autumn, winter and spring. *Hollingsworth et al.* [1996] found enhanced temperature variance in Acidalia, Arcadia, and Utopia, and suggested that these Martian storm zones were controlled by the topography. *Hollingsworth et al.* [1997] further studied the seasonal cycle of storm zones on Mars, and found that Martian storm zones could occur in northern autumn, winter and spring, with the springtime variance being the strongest. *Wilson et al.* [2002] identified a fast (6–7 sol) and a slow (~20 sol) eastward traveling zonal wave number m = 1 in the midlevel air temperatures in the northern hemisphere of Mars using MGS TES data. They simulated traveling waves using the GFDL Mars GCM, and stated that simulations typically yield traveling waves of zonal wave 1, 2 and 3 with periods of 7, 3–4, and ~2 sols, respectively, which are consistent with Viking lander observations and modeling work by *Barnes et al.* [1993]. They also pointed out that the simulated waves 2 and 3 are shallow features, and all the "fast" waves have temperature maxima at low levels (at the steering level), a westward phase tilt with height, features which are consistent with baroclinically unstable waves. *Banfield et al.* [2004] cataloged the behavior of different modes of transient waves in TES data. They found that m = 2 and m = 3 were confined nearer the surface than m = 1. They also found that in the northern hemisphere, m = 2 and m = 3 were more evident in the fall and spring, while m = 1 dominated the period around northern winter solstice.

[12] While much work has been done studying observations and models of transient wave activity, the linkage between these waves and observed fronts is much weaker, and the current paper is an attempt to fill this gap. In the next section, we first discuss the identification of dust fronts in the MOC data, providing examples, then present statistics on the seasonal and spatial distribution of frontal dust storms over the course of two Martian years. In section 4, we examine the correlation between the seasonal and spatial patterns of frontal dust storm development and of transient wave activity. Having provided some evidence of this correlation, in section 4.4, we attempt to explain the relationship between the seasonal variation of frontal development and the seasonal variation of the structure of the polar vortex.

2. Mars Orbiter Camera Data and Frontal Storm Identification

[13] In this study, we employed both MGS MOC and TES data. The analyzed data covered the period from June 1999 (Ls ~ 150°) to September 2003 (Ls ~ 270°), corresponding to ~2.3 Martian years. MGS is in a 2-hour, nearly sun-synchronous, and nearly circular mapping orbit [*Albee et al.*, 2001]. During the course of each orbit, the MOC wide-angle push-broom cameras built a pair of global map swaths in red and blue filters at a resolution of roughly 7.5 or 3.75 km/pixel (depending on across-track summation mode) [*Malin and Edgett*, 2001; *Cantor et al.*, 2001; *Wang and Ingersoll*, 2002]. At the same time, TES collected spectra from 200 to 1600 cm^{-1} (6–50 micron) at spectral resolutions of 10 or 5 cm^{-1}, usually oriented nadir, with surface resolutions of roughly 6–10 km, with six instantaneous pixels [*Christensen et al.*, 2001]. TES data are used to study temperature perturbations associated with frontal storms, and are introduced in section 4.

[14] Mars daily global maps were made from MOC global map swaths following the method described by *Wang and Ingersoll* [2002]. We have used these daily global maps to identify dust and/or condensate cloud bands, which appear similar to terrestrial baroclinic fronts. Examples of many of these different kinds of features are shown in Figure 1, which provides a visual definition for the concepts and feature categorizations used here, such as streak *vs*. front. With dust fronts identified on the basis of linear or curved band morphology, we assign a unique identification (ID) number to each identified feature, and record the position of the southern edge and the corresponding Ls. In this way, a catalog of frontal storm occurrence as a function of location and season has been built up. We have further subclassified the features according to whether they were composed of dust or water ice (a categorization based on color), whether they showed apparent southward motion (i.e., for dust fronts whether the storm flushes dust southward), whether the feature was new or had been identified on previous days, whether the front was detached from the polar cap/hood edge, whether the front could have been related to topographic slope winds rather than a propagating front, and whether the front could have been a streak rather than a front. Fronts that were clearly persistent in the images

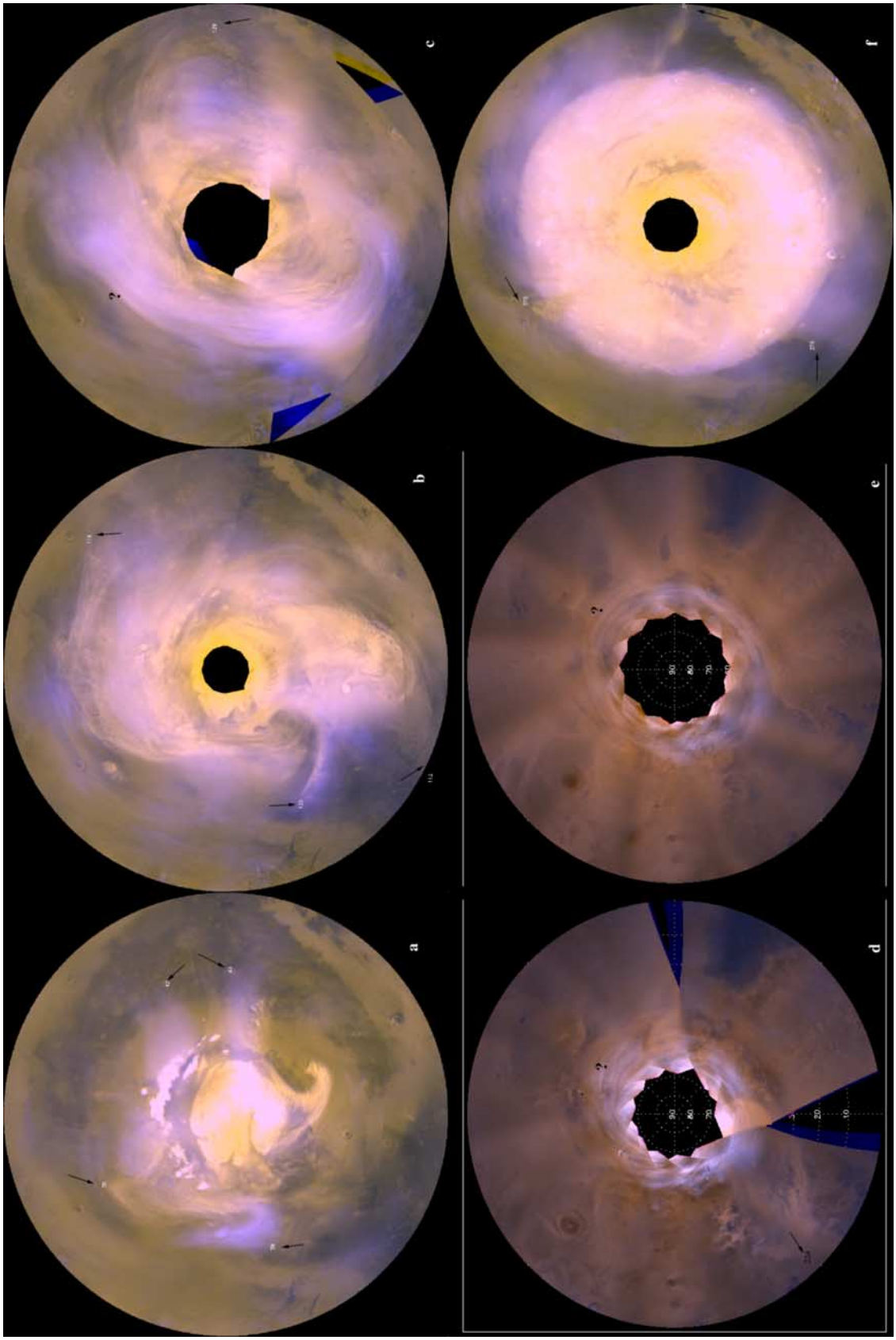

Figure 1

for more than one day (multiday events) were identified with the aid of animated daily global maps and were tagged with the same ID that was assigned when that feature was first identified. We continued to track such features even if the original frontal appearance was lost and regardless of the underlying drive for subsequent movement (the nature of which could generally only be speculated). For events that involved both dust and condensate clouds, we recorded the event as both a dust and an ice clouds event. Given that the identification of features in the images is a subjective process, we examined the images twice in the time order of collection, and once again with random time ordering (in order to minimize creeping changes in feature definitions and criteria). Only events that were recorded in all three passes through the data were included in the catalog.

3. MOC Frontal Storm Statistics

[15] Results from the first MGS mapping year (MY 24, 1999–2001) of the MOC frontal storm survey are shown in Figure 2. The plotted data points correspond to the southern edges of dust fronts that are listed as new dust events in the catalog. The spatial distribution data show that most of the frontal dust storms were concentrated in the low topographic regions of Acidalia, Arcadia and Utopia. Using GCM simulations, *Hollingsworth et al.* [1996] has shown that these regions are storm zones in the northern hemisphere of Mars. The middle panel shows the latitudinal and seasonal distribution of frontal dust storms from late northern summer (Ls = 150°) to the northern summer solstice of the next Martian year (Ls = 90°). A striking feature in this plot is the absence of storms in a period centered on the northern winter solstice (Ls 240°–Ls 300°, solstice at Ls 270°). During the solstice period, many streaks such as those in Figure 1e were observed in the polar hood, however, none showed any clear frontal features such as those seen in Figures 1b, 1c, and 1d. Away from the solstice period, the latitudes of frontal dust storms appear to follow the trend indicated by the terminator curve (latitude of the edge of polar night). Though we did not measure the size of the storm explicitly, the distance between the terminator and the southern edge of the storm can serve as a proxy for the meridional extent of the storm from early fall to midwinter. Note that the polar cap is very extensive in late winter and early spring. As a result, the extent of the polar cap is much larger than the extent of the polar night (Figure 1f). In this case, the size of the storm is better measured from the edge of the polar cap. Interestingly, the largest of the frontal storms that transported dust to the low latitudes (e.g., Figure 1d) occurred just before and just after the no-storm period. We will refer to such large frontal dust storms as "flushing storms" [*Wang et al.*, 2003]. The histogram of the occurrence data shows maxima during the periods Ls = 160°–170° and 190°–230°. During the Ls = 210°–230° period, repeated flushing storms transported dust from the northern hemisphere to the southern subtropics through the Acidalia-Chryse channel, and resulted in global impact on the atmospheric thermal structure in the first MGS mapping year [*Wang et al.*, 2003]. The sequence of flushing dust storms was followed by an abrupt cessation of frontal dust storm activity after $L_s \sim 230°$. This reminds us of the rapid reduction of transient eddy activity right after the $L_s \sim 270°$ 1977b global dust storm [*Barnes*, 1980]. In the postsolstice period of MY 24, the occurrence frequency of storms shows a broad peak in late northern winter.

[16] Occurrence data for the second MGS mapping year (MY 25, 2001–2003) are shown in Figure 3. In this Martian year, a global dust storm developed, which originated near the Hellas basin around Ls ∼ 182°, peaked around Ls ∼ 210°, and dissipated by Ls ∼ 240° [*Smith et al.*, 2002; *Strausberg et al.*, 2005]. Despite the global dust storm, the data on frontal dust storm activity show some similar occurrence patterns in the geographical and seasonal distributions of frontal dust storms as those for the first MGS mapping year. Many fronts were observed around the north polar cap shortly after the onset of the global dust storm. The frontal storm shut-off date in this year (Ls ∼ 220°) is earlier than that in the previous year (Ls ∼ 230°). The global dust storm caused ∼30 K warming at 0.5 mb over 10 days after the storm onset, and ∼40 K warming at the peak of the storm compared to the previous year [*Smith et al.*, 2002]. If there is a "threshold" thermal state characterized by large atmospheric static stability for the suppression of frontal dust storms, it should arrive earlier in the fall of MY 25 than in the fall of MY 24. This appears consistent with the earlier frontal dust storm shut-off this year. The gradual shut-off of frontal dust storms after the onset of the Ls ∼ 182° 2001 global dust storm is in contrast with the sudden reduction of transient eddies after the $L_s \sim 270°$ 1977b global dust storm, but somewhat similar to the situation after the $L_s \sim 205°$ 1977a global dust storm where no apparent transient eddy suppression was observed [*Barnes*, 1980]. The 1977a global dust storm had a shorter duration and the storm dissipated well before $L_s \sim 240°$. The discussion above appears to imply that the time lag between the onset of a

Figure 1. A variety of polar stereographically projected daily global maps encountered during storm identification. Figures 1d and 1e cover the whole northern hemisphere, while the others cover the area north of 45°N. Identified frontal storms are indicated by arrows pointing to their ID numbers at the southern edges of the events in the images. All examples are taken from the first MGS mapping year (MY 24, 1999–2001), but they span the range of morphologies for all our data. Figures 1a and 1e show examples of small fronts scattered around the polar cap. Their morphologies range from linear dust bands extending southward from the polar cap (Figure 1e) to various kinds of curved bands around the cap edge (Figure 1a). Figures 1b, 1c, and 1d show large storms possessing classical frontal features characteristic of terrestrial baroclinic storms. The feature indicated by the question mark in Figure 1c appears as a streak that extends more than half a circumstance around the pole. It is possibly formed by stretching a former front by strong winds. Such long streaky features do not count in the catalog. The question marks in Figures 1d and 1e refer to the numerous thin streaks that appear to be circling around or spiraling into the pole. These streaks in the polar hood are not included in the catalog, either. The Ls values are (a) 162°, (b) 184°, (c) 188°, (d) 221°, (e) 242°, and (f) 357°.

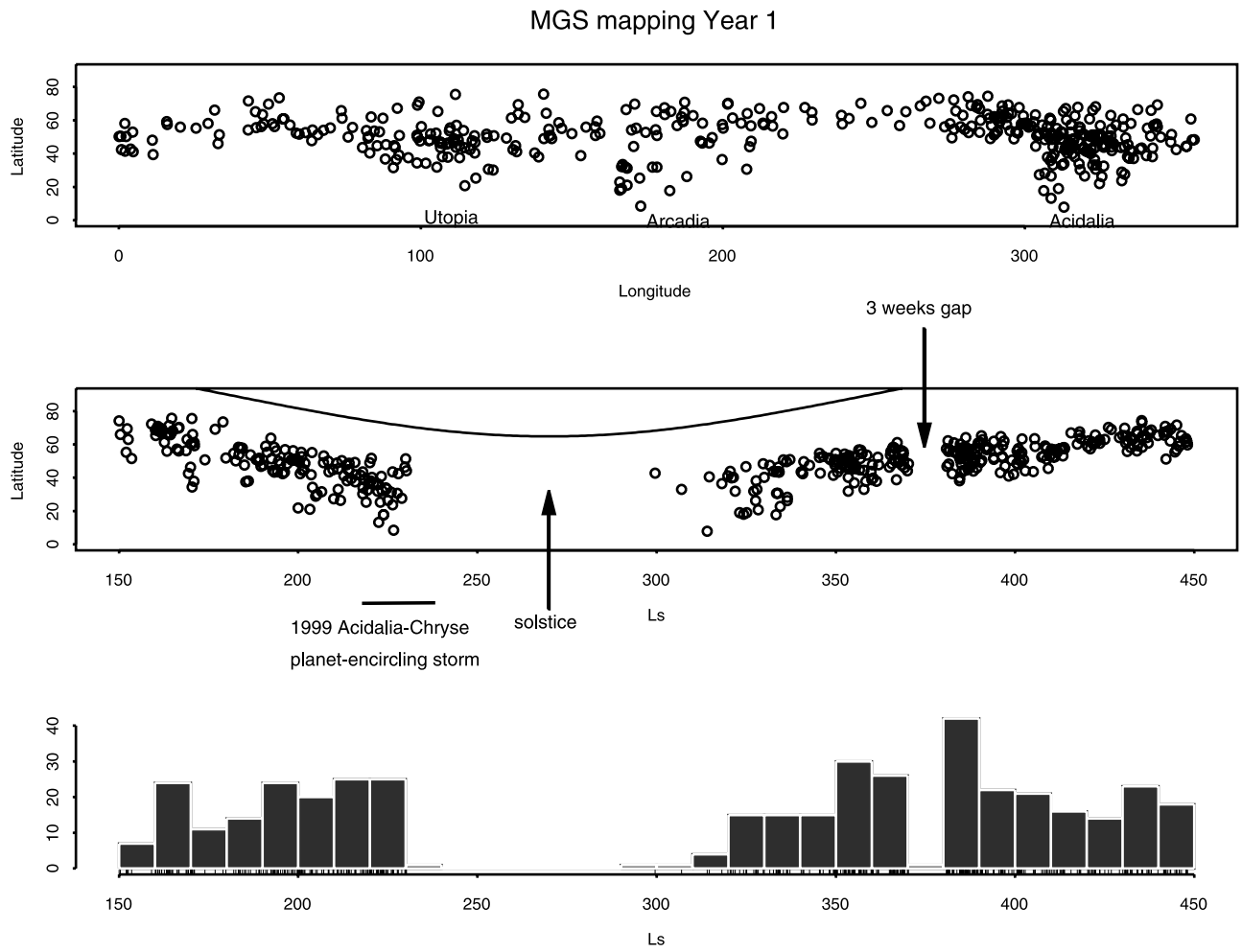

Figure 2. Spatial and temporal distributions of frontal dust storms in MGS mapping Year 1 (MY 24, 1999–2001). The plotted data points correspond to the southern edges of dust fronts that were listed as new dust events in the catalog. The spatial distribution data show that most of the frontal dust storms were concentrated in the low topographic regions of Acidalia, Arcadia, and Utopia. The middle panel shows the latitudinal and seasonal distribution of frontal dust storms from late northern summer (L_s = 150°) to the northern summer solstice of the next Martian year (L_s = 90°). Periods with missing data are indicated in the figure. The curve corresponds to the edge of polar night (terminator). The bottom panel is a histogram showing the number of storms within each 10° L_s bin as a function of L_s.

global storm and the reduction of transient eddy activity relates to the timing and duration/strength of the global dust storm, with shorter time lag for more vigorous global dust storm that occurs nearer to the northern winter solstice. In the early phase of the 2001 global dust storm, several dust fronts reached the midlatitudes, but no large flushing fronts were observed in the later part of the global storm. On the one hand, this may be due to the fact that at the peak of the global storm, the very thick dust haze south of the northern polar region made it difficult to identify dust fronts in the low latitudes. On the other hand, increased static stability and the strengthened polar jet may have suppressed baroclinic storms.

[17] The distribution of flushing dust fronts observed from 1999 to 2003 (MY 24–26) is shown in Figure 4. This figure highlights the solstice gap in the seasonal distribution evident in all three years of MGS observations (and to this degree a robust feature). Large flushing storms generally occur during two windows, one at L_s = 200°–240° and the other at L_s = 300°–340°. These frontal storms can transport dust from the northern mid and high latitudes well into the low latitudes, and sometimes across the equator and into the southern midlatitudes. Much less frequently, in early fall and early spring, large flushing storms can also transport dust to latitudes as low as ~25°N. The majority of such flushing events occur in the Acidalia channel, but the other two low topographic channels, associated with Arcadia and Utopia, are also hosts to quite a number of flushing storms. In the presolstice period of Year 3, the most active channel was Utopia.

[18] Examples of flushing fronts are shown in Figure 5 for each of the three channels. Figure 5g shows a Utopia flushing dust storm that transported dust to ~25°N at L_s ~ 206°. It was one of a sequence of similar events. In the following week, dust was tracked to the equator. At L_s ~ 212°, this dust was augmented by material lifted by another dust storm, and eventually the dust reached northern Hellas. Figure 5f shows another flushing storm in Utopia, but at

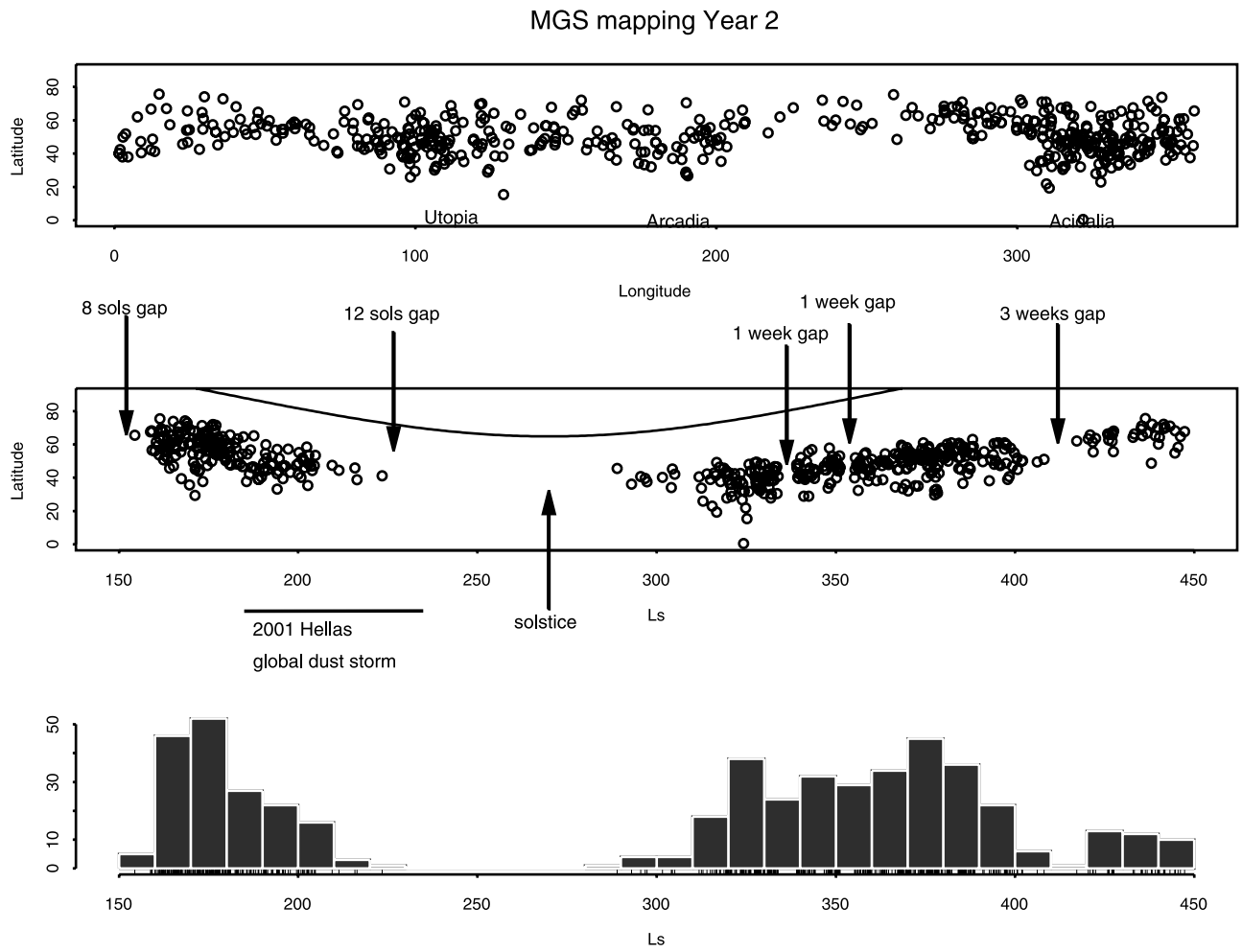

Figure 3. Spatial and temporal distributions of frontal dust storms in MGS mapping Year 2 (MY 25, 2001–2003). The top panel shows the latitude-(east) longitude distribution of the southern edges of the storms. The middle panel shows the latitude-*Ls* distribution of the southern edges of the storms. The curve corresponds to the edge of polar night. The bottom panel is a histogram showing the number of frontal dust storms in 10° *Ls* bin as a function of *Ls*. Data gaps and northern winter solstice (*Ls* = 270°) are annotated and indicated by arrows. The time period for the Hellas global dust storm is indicated by the thick line under the horizontal axis of the middle panel.

Ls ∼ 324° in MGS Year 2. A representative flushing storm in Arcadia is shown in Figure 5c. Arcadia dust fronts are usually orientated in a more north-south direction than those in the other two channels. Other panels in Figure 5 show examples of Acidalia flushing dust storms in different seasons and years. White arrows in Figures 5a, 5d, 5e, and 5h point to dust patches/bands south of the main frontal bands. These are probably associated with dust flushed southward by previous flushing storms in the channel or perhaps, with newly lifted dust ahead of the original flushing storm [*Wang et al.*, 2003].

4. Transient Eddies Observed by the Thermal Emission Spectrometer

[19] Atmospheric vertical temperature profiles derived from the TES spectra are obtained from the Planetary Data System [*Conrath et al.*, 2000]. The temperatures are provided on 38 pressure levels between 16.582 mb and 0.0016 mb, and are stored in "ATM" tables as a part of the standard TES products. In order to test the fidelity of TES retrievals in the lower atmosphere, *Hinson et al.* [2004] compared MGS TES temperature profiles with nearly simultaneous MGS Radio Science (RS) occultation temperature profiles at the same locations. They found temperatures retrieved with the two instruments and techniques to agree to within ∼2 K for pressures <400 Pa, while TES temperatures at 610 Pa are generally ∼2–8 K warmer than RS temperatures. Since perturbations of TES temperatures are relative temperature changes at fixed pressure level, the absolute temperatures are not so critical. Note that traveling waves have been found in both TES and RS data [*Wilson et al.*, 2002; *Banfield et al.*, 2004; *Hinson and Wilson*, 2002]. Since the RS data are tempo-

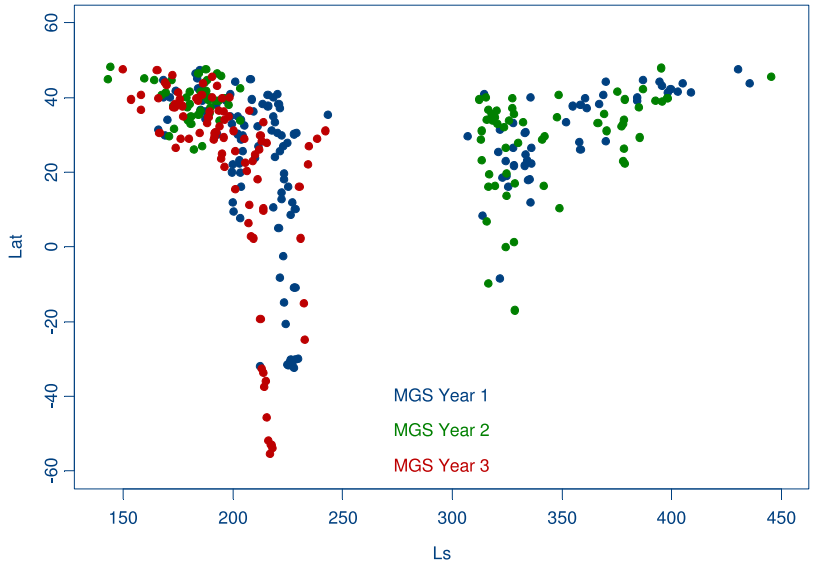

Figure 4. Distribution in latitude and seasonal date (*Ls*) plot of the southern tips of frontal dust storms observed in MOC images to transport dust southward. Blue dots are for MGS mapping Year 1 (1999–2001), green are for Year 2 (2001–2003), and red are for Year 3 (2003–2005). The currently analyzed data last until *Ls* 270° in Year 3. Figure 4 does not include storms that only travel around the polar region but do not transport dust southward. Multiday events get multiple dots in Figure 4, with one dot for each day, while in Figures 2 and 3, multiday events only get one dot corresponding to the first day.

rally and spatially sparse, they are not suitable for the current study.

4.1. Temperature Anomalies Associated With Flushing Storms

[20] By analogy with terrestrial weather systems, it would seem reasonable to hypothesize that the observed dust bands delineate fronts that are associated with instabilities in the atmosphere, and likely with baroclinic instability. This hypothesis suggests that the fronts should be directly related to thermal perturbations in the atmosphere, and specifically with the patterns of warm and cold sectors observed in terrestrial cyclones. In order to search for such temperature anomalies associated with frontal storms, we have calculated day-time temperature perturbations at each vertical level along the TES observation track. For each track on the day side, we first bin TES temperatures along the tracks by 1° latitude. A mean and standard deviation is constructed for each bin using all the data (at a given level) that lie within 15° longitude and 1° latitude of the bin center, and that are available for 50 MGS orbits (~100 hours) on either side of the bin center. The means are subtracted from the temperatures at the bin centers to get temperature anomalies. The significance of the anomaly is gauged by comparison with the standard deviation. An example for *Ls* ~ 209° in Year 1 is shown in Figure 6. Temperature anomalies at 4.75 mb along TES tracks are color coded and superimposed on polar stereographically projected Mars daily global maps (0°N–90°N), which are composed using the global map swaths obtained from the same MGS orbits. The numbers next to the tracks are the 13 sequential track numbers from which this daily global map is constructed. Tracks 5 and 6 cut across the dust front indicated by the arrow. Large negative temperature anomalies are observed north of and behind the dust band, suggesting that dust is located within the cold sector behind or adjacent to a cold front. The extreme temperature anomaly in this case is ~−20 K, and the corresponding standard deviation is ~−10 K. The temperature anomalies are largest near the surface and decrease with altitude. The anomalies become comparable to the standard deviations by 2.24 mb, indicating that signatures of baroclinic storms were confined to the lower atmosphere.

[21] We have summarized the 6.1 mb temperature perturbation results for flushing storms in Figure 7. The horizontal axis is the extreme temperature perturbations (ΔT) along the tracks that cut across frontal dust storms. The vertical axis is the standard deviation of transient temperature perturbations for the bin into which that temperature falls over the 50 orbits range, as defined above. Note this figure contains many fewer data points than Figures 2 and 3 because it does not include small frontal storms. The lines in Figure 7 correspond to ±1 and ±2 standard deviations (σ). If a track shows only one extreme point (either positive or negative anomaly), the extreme point is recorded. In cases where a track shows both positive and negative anomalies, we do the following: if the absolute values of the anomalies are both larger or both smaller than the standard deviation, then the anomaly with the larger absolute value is recorded; otherwise, the one with the absolute value larger than the standard deviation is recorded. The 6.1 mb temperature anomalies (ΔT) associated with the flushing storms range between ±20K. The proportion of points within different sectors of Figure 7 is summarized in the first row of Table 1. Points (ΔT) that lie outside of the sector between −σ and σ are above one standard deviation compared to natural transient temperature perturbations (T') in that bin (defined above). The second row of Table 1 lists the proportion expected for a Gaussian (random) process. Table 1 shows that 52% of the observed ΔTs lie below −σ, and 9% lie

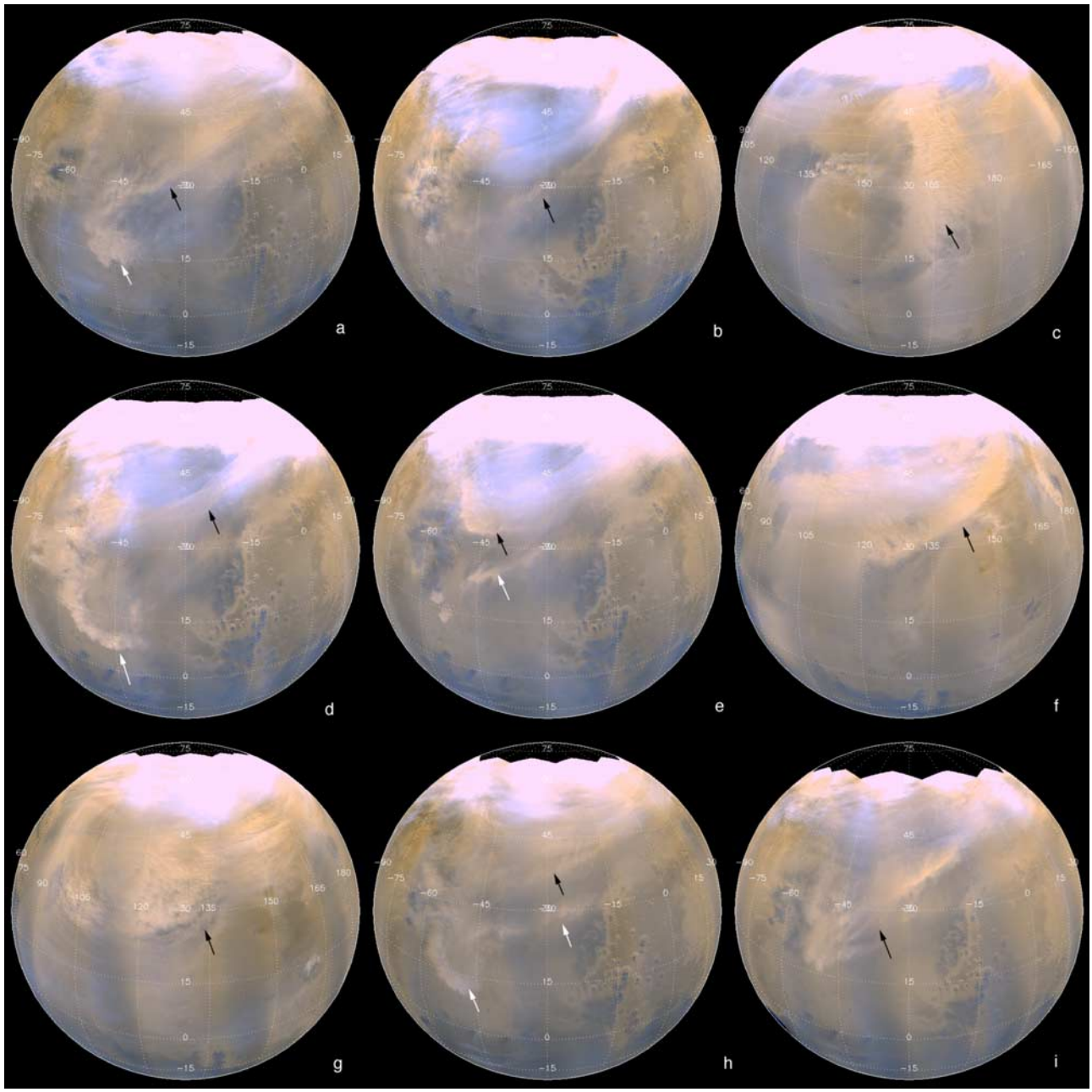

Figure 5. Examples of flushing dust storms in different channels, seasons, and years. Each panel is a Mars daily global map projected onto a sphere with black arrows pointing to the main frontal features. The three rows from the top to the bottom are for MGS mapping Years 1 (1999–2001), 2 (2001–2003), and 3 (2003–2005), respectively. Figures 5a, 5b, 5d, 5e, 5h, and 5i are for the Acidalia channel. Figure 5c is for the Arcadia channel. Figures 5f and 5g are for the Utopia channel. The *L*s values are (a) 210°, (b) 314°, (c) 336°, (d) 316°, (e) 324°, (f) 324°, (g) 207°, (h) 214°, and (i) 230°.

below -2σ. For comparison, in a Gaussian distribution, only 16% of data should lie below $-\sigma$, and only 2.3% should lie below -2σ. The mean of the recorded ΔTs is -3.84 K, and the standard deviation of recorded ΔTs is 8.89 K. The spread in ΔT is partially related to the vertical structure and development stage of different event. For example, a baroclinic storm confined near the ground may not be tall enough to reach the examined 6.1 mb surface and leave the expected thermal signature (Note the surface pressure in the northern plains is larger than 6.1 mb), a baroclinic storm near the end of its lifecycle will have very small temperature deviation, the heating effect of dust may produce positive temperature perturbation at certain levels. There are $n = 147$ data points in Figure 7. A Student's t test with a null hypothesis H0: $\Delta T < 0$ (i.e., that there is negative temperature anomaly associated with flushing storms) gives

$$X = \frac{\Delta T}{stdev(\Delta T) \times \sqrt{n-1}} = \frac{-3.84}{8.89\sqrt{147-1}} \approx -5.24 < -2.35,$$

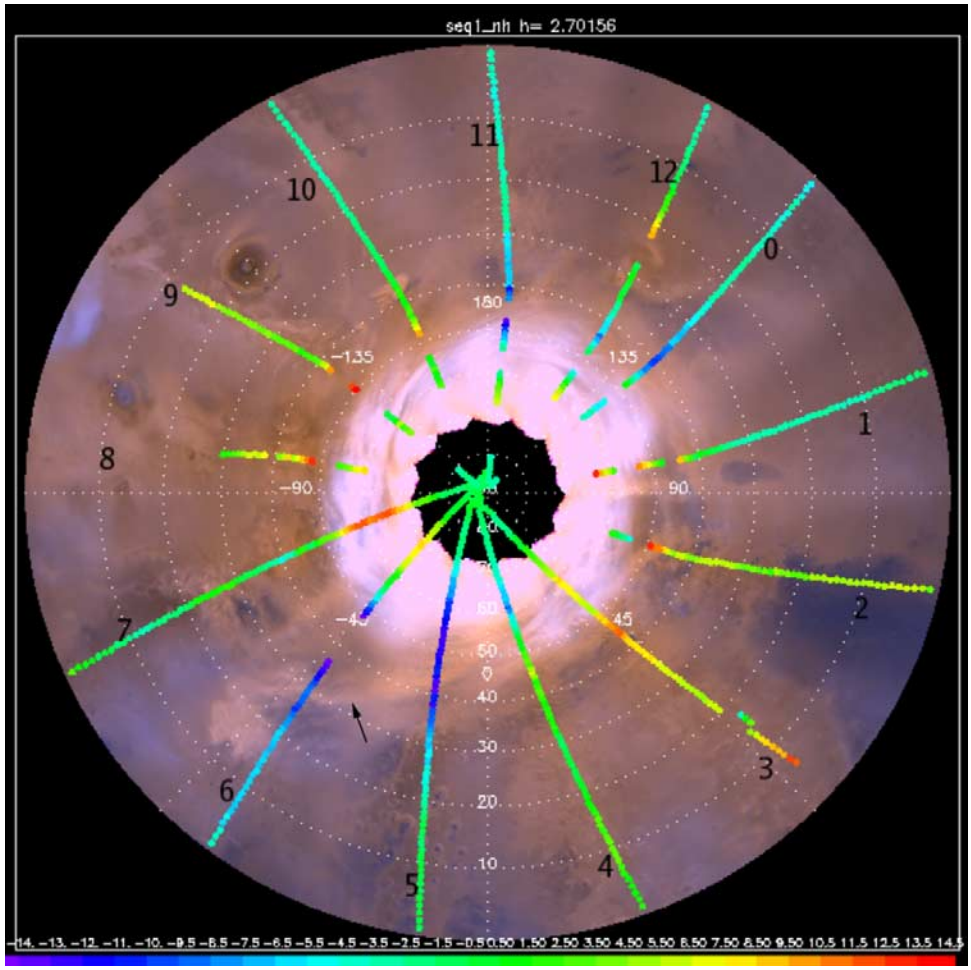

Figure 6. Temperature anomalies at 4.75 mb along TES tracks for the daily global maps (0°–90°N) at *Ls* ~210° in MGS mapping Year 1. The individual images used for this daily global map are m0703841, m0703847, m0703857, m0703878, m0703916, m0703954, m0703982, m0704016, m0704045, m0704051, m0704061, m0704065, m0704071 and their corresponding blue images. East longitudes are shown along 45°N, and north latitudes are shown along 0° longitude. The numbers 0–12 next to the tracks are track IDs for this map.

where −2.35 is the lower 1% percentile of a Student's t distribution with 146 degrees of freedom. (The percentile can be obtained either through looking up the corresponding statistical table for Student's T distribution or through statistical software such as Splus. For example, qt(0.01, 146) in Splus outputs the lower 1% percentile of the Student's T distribution with 146 degrees of freedom.) Therefore we accept the null hypothesis at a 1% significance level. This statistical analysis shows that there is a high degree of confidence that the observed data are consistent with cold temperatures being associated with flushing frontal storms. It should be noted that large overlying dust opacity can depress surface temperatures substantially (R. J. Wilson, personal communication, 2005). Therefore it is possible that all dust events would be characterized by cold temperatures independent of the atmospheric circulation. However, in most cases, cold temperatures span the whole region north of the dust band, not just over the band itself (e.g., Figure 6). So, it is reasonable that the dust band is near the interface of cold and warm air masses.

4.2. Seasonality of Transient Temperature Perturbations and Frontal Storms

[22] The baroclinic hypothesis for the development of visible fronts argues for a relationship between the behavior of these fronts as revealed in the frontal storm catalog and the distribution of transient eddies as revealed by TES thermal measurements. To test this, we calculated transient temperature perturbation standard deviations for a range of seasonal dates. *Banfield et al.* [2004] have described traveling waves in the Martian atmosphere using MGS TES nadir data. We present similar analyses here, but with specific emphasis on their relationship to fronts. We calculated the standard deviation for daytime TES temperatures within grid boxes of 15° longitude by 2° latitude by 30° *Ls*. A 5th-degree polynomial temporal trend is removed from the time series at each grid box before the standard deviation is calculated in order to remove slow seasonal temperature variation due to quasi-stationary waves.

[23] The top three panels of Figure 8 show zonally averaged standard deviation of temperature at 4.75 mb as a function of *Ls* and latitude for MGS Year 1, 2, and 3 (MY

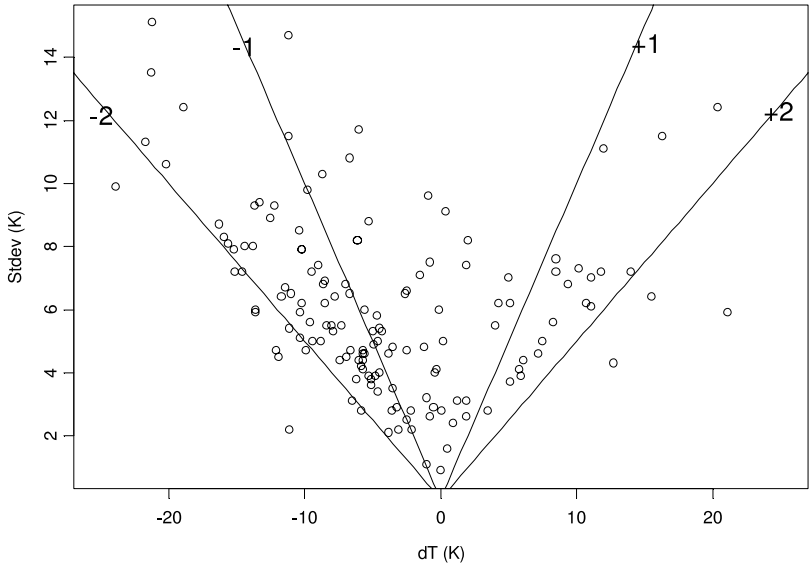

Figure 7. Temperature anomalies associated with frontal dust storms at 6.1 mb. The horizontal axis is temperature anomaly. The vertical axis is the standard deviation of the temperature anomaly. The lines correspond to $\pm\sigma$ and $\pm 2\sigma$.

24–26). Stronger eddy activity is seen to have occurred before and after the solstice period. This pattern shows great similarity to that obtained for frontal dust storms observed in images (see Figures 2, 3, and 4), suggesting that the meteorological systems associated with these fronts contribute significantly to the standard deviation of temperature. In the presolstice period, eddy activity is the weakest in the second mapping year, consistent with frontal activity being suppressed during the 2001 global dust storm. Stronger eddy activity is observed in the autumn of the third year than in the autumns of either of the previous two years. This is perhaps related to the overall weaker static stability in the presolstice period of the third year (see below and Figure 9). We also counted more frontal storms in the autumn of the third year than in the previous two autumns (not shown). The bottom three panels of Figure 8 show zonally averaged standard deviation at 2.24 mb. The seasonal distribution of eddy activity at this level significantly differs from that for the frontal storms. The fact that the strong, double peaked pattern evident at the 4.75 mb level disappears at 2.24 mb suggests that the eddies responsible for the lower level patterns (and by extension, the dust fronts) are confined to lower levels. *Banfield et al.* [2004] noticed very strong m = 1 traveling wave activity in the upper atmosphere (say 0.5 mb) that peaks in the solstice season. *Wilson et al.* [2002] argues that it is a barotropic energy conversion and that the traveling waves are associated with inertially unstable regions at low latitudes. We will discuss different wave modes evident in the TES data further in section 4.4.

[24] Figure 9 shows the seasonal distribution of several parameters related to baroclinic instability theory and derived from the zonal mean TES temperatures. The left column corresponds to 4.75 mb, and the right column corresponds to 2.24 mb. The top row shows the latitude of polar vortex edge which is defined as the latitude corresponding to the minimum latitudinal temperature gradient ($\frac{dT}{dy}$) between 30°N and 80°N. In general, the polar vortex is about 6° in latitude closer to the pole during the winter solstice period than it is during early-mid fall and mid-late winter. Row 2 shows $\frac{dT}{dy}$ at the vortex edge. The temperature gradient maximizes during Ls 260°–Ls 300° due to the enhanced polar radiative cooling and the midlatitude adiabatic warming associated with the descending branch of the Hadley circulation during the winter solstice period. The range of temperature gradient variation is larger at the upper level than at the lower level. Row 3 shows the static stability parameter squared (N^{*2} is also the Brunt-Vaisalla frequency squared) at the vortex edge. It maximizes during Ls 230°–Ls 270° due to the greater poleward slope with height of the polar vortex boundary during the winter solstice period. The global dust storm in MGS Year 2 lifted the atmospheric stability in the presolstice period over that in

Table 1. Proportion of Data Within Different Sectors[a]

	$X < -\sigma$	$-\sigma < X < \sigma$	$X > \sigma$	$X < -2\sigma$	$-2\sigma < X < 2\sigma$	$X > 2\sigma$
ΔT	52%	47%	16%	9%	89%	2%
Gaussian	16%	68%	16%	2.3%	95.4%	2.3%

[a]See Figure 7. The data are for the actual distribution of observed extreme temperature anomalies (the second row of the table) and (for comparison) the Gaussian (random) distribution (the third row of the table). The fact that 52% (many more than 16%) of the observations are within the $X < -\sigma$ sector suggests a statistically significant correlation of negative temperatures with the trailing air mass of observed fronts.

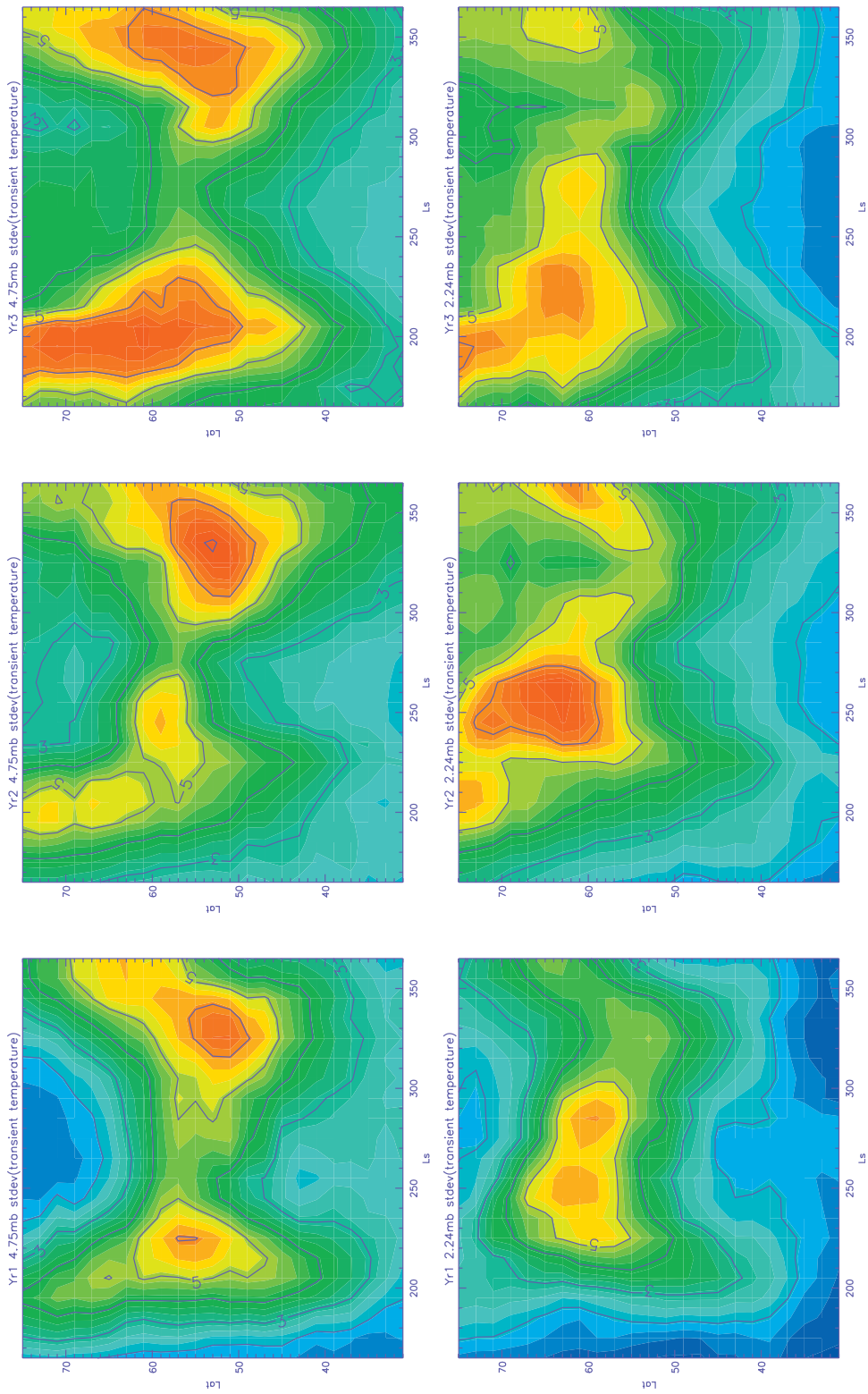

Figure 8. Standard deviations of daytime transient temperature perturbations as a function of L_s and latitude. The top row is for 4.75 mb, and the bottom row for 2.24 mb. The columns from left to right correspond to MGS mapping Years 1 (1999–2001), 2 (2001–2003), and 3 (2003–2005), respectively.

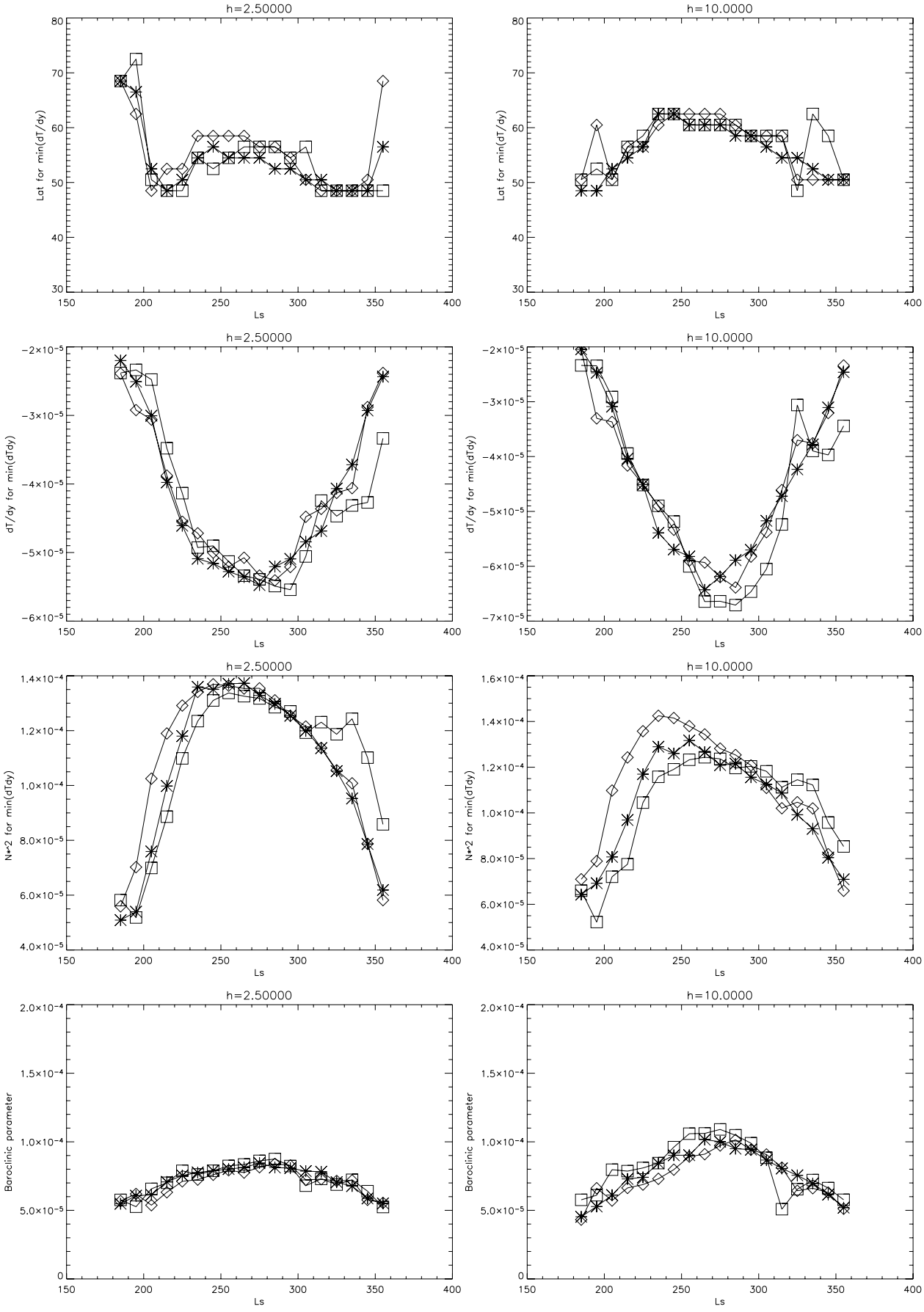
h=2.50000
h=10.0000
Lat for min(dT/dy)
dT/dy for min(dTdy)
N**2 for min(dTdy)
Baroclinic parameter
Ls

Figure 9

the other two years, especially at upper levels. MGS Year 3 has the smallest fall-time static stability in the three years. However, the winter-time stability in MGS Year 3 is substantially larger than the other two. This is associated with the regional dust storm in December 2003, before the landing of Mars Exploration Rovers (MER). Row 4 of Figure 9 shows the baroclinic parameter $\left(\alpha = \frac{f(du/dz)}{N^*} = \frac{R(dT/dy)}{H \cdot N^*}\right)$ at the vortex edge, where f is the Coriolis parameter, H is the scale height. The combined behaviors of $\frac{dT}{dy}$ in Row 2 and N^{*2} in Row 3 result in a more symmetric seasonal variation of the baroclinic parameter (α) which maximizes at the northern winter solstice. The baroclinic parameter is proportional to the maximum growth rate of baroclinic instabilities [*Lindzen and Farrell*, 1980]. The baroclinicity of the atmosphere is the strongest around northern winter solstice. However, eddies in the lower atmosphere are actually weaker during the solstice period. At upper levels, the strongest baroclinicity still occurs at Ls $\sim 270°$. While eddies in MGS Year 1 (MY 24) appear to be centered on the solstice, eddies in MGS Year 2 maximize during Ls 240°–260°, and eddies in MGS Year 3 maximize even earlier than MGS Year 2. So, there is not much correlation between the baroclinic parameter and the eddy activity at upper levels. Note that the expression for the baroclinic parameter α is derived for quasigeostrophic instability. Therefore it is not exactly valid for the region with very strong jet on Mars that is characterized by Rossby number $Ro \geq 1$. Also note that the coarse vertical resolution (~5 km) of TES data prevents us from calculating N^{*2} accurately. MGS radio science data with a much finer vertical resolution (200 m) show that there are fine structures in the vertical temperature profiles [*Hinson et al.*, 2004]. During the cold season, sometimes there are near surface temperature inversion layers that cannot be resolved by TES, leading to lower atmospheric static stability calculated on the basis of TES data.

4.3. Flushing Storms and Storm Tracks

[25] Figure 10 shows the latitude-(east) longitude distribution of transient temperature RMS amplitude at 4.75 mb for selected 30° Ls periods of MGS Year 1 (MY 24). Figure 10a corresponds to the period before the formation of north polar hood. The vortex edge temperature gradient is sharpening as the northern fall approaches. Compared to the other panels in the figure, this period does not have much eddy activity between 0° and 76°N. Figures 10c and 10d correspond to the solstice period. Images for this period show streaks in the polar hood, but no frontal storms (Figure 1). This period has the strongest baroclinicity, but the weakest eddy activity in the lower atmosphere. Eddy activities are concentrated in a thin circumpolar band about 6° wide in latitude with a zonal wave number two pattern at the edge of the polar vortex. Figures 10b, 10e, and 10f correspond to the presolstice and postsolstice periods when regional scale flushing dust storms transport dust from the northern mid-high latitudes to the low latitudes. Examples of such storms are shown in Figure 5. Significant eddy activities apparently span a wider latitudinal band (~12° latitude in most places) in these periods. Moreover, large standard deviations are evident in/near low topographic channels, especially in Tempe Terra and Acidalia (270°E–360°E) where most of the flushing storms are observed in MGS Year 1. Consistent with the large spatial scale of flushing storms, the spikes in standard deviations are also elongated in the north-south direction. The Acidalia sector appears like a storm zone due to the locally larger temperature variations. *Hollingsworth et al.* [1996] investigated Martian storm zones using NASA Ames GCM, and pointed out that topography played a dominant role in localizing transient eddy activity to Acidalia, Arcadia and Utopia. GCM results show strong transient baroclinic eddies during northern autumn, winter and spring, with the winter solstice storm zones being weaker [*Barnes et al.*, 1993; *Hollingsworth et al.*, 1997; *Wang et al.*, 2003, S. Basu et al., Simulation of spontaneous and variable global dust storms with the GFDL Mars GCM, manuscript in preparation, 2005 (hereinafter referred to as Basu et al., manuscript in preparation, 2005)]. Our study suggests that the largest enhancement of the localized transient temperature anomalies is associated with flushing storms which are the largest frontal dust storms.

[26] A plot similar to Figure 10 can be found in Figure 20 of *Banfield et al.* [2004] for MGS Year 2 (MY 25). Note that they plotted the area north of 10°N. Their figure shows that strong storm zones are evident in Acidalia during mid to late northern winter. This is in nice agreement with the timing and location of the observed flushing storms. No such eddy activity centers are observed in the presolstice period when the global dust storm (in MGS Year 2, MY 25) dramatically increased the atmospheric static stability.

[27] Figure 11 is similar to Figure 10, but for MGS Year 3 (MY 26). Weaker eddies in the winter solstice period is sandwiched between stronger eddies in the fall and winter. In agreement with the elevated eddy activity in Utopia in the presolstice period, MOC observations show that flushing storms are especially active in the Utopia channel (70°E–70°E) this fall. An example is shown in Figure 5 and discussed in section 3. The Acidalia-Chryse channel shows more activity in the postsolstice period. This is consistent with the regional dust storm in December 2003 (before the MER landing). It is possible that this regional dust storm was related to flushing events. We have yet to process images after Ls 270° in the third year to see exactly what happened in the postsolstice period.

[28] MGS observations show that the minimum in the seasonal cycle of eddy temperatures and frontal dust storms occur when the atmosphere is deemed more unstable to linear baroclinic instability. This is somewhat analogous to the terrestrial midwinter suppression of baroclinic wave

Figure 9. Parameters derived from the zonal mean TES temperature data. The left column is for 4.75 mb (i.e., a log-pressure height of 2.5 km). The right column is for 2.24 mb (10 km). Diamonds are for MGS mapping Year 1 (MY 24, 1999–2001), stars are for Year 2, and squares are for Year 3. The horizontal axis for each panel is Ls. The first row from the top is the latitude of the edge of polar vortex defined as the latitude that corresponds to the minimum $\frac{dT}{dy}$. The second row is the value of $\frac{dT}{dy}$ at the vortex edge. The third row is the static stability squared (N^{*2}) at the vortex edge. The fourth row is the baroclinic parameter (α) which is proportional to the maximum baroclinic instability growth rate for quasigeostrophic flow.

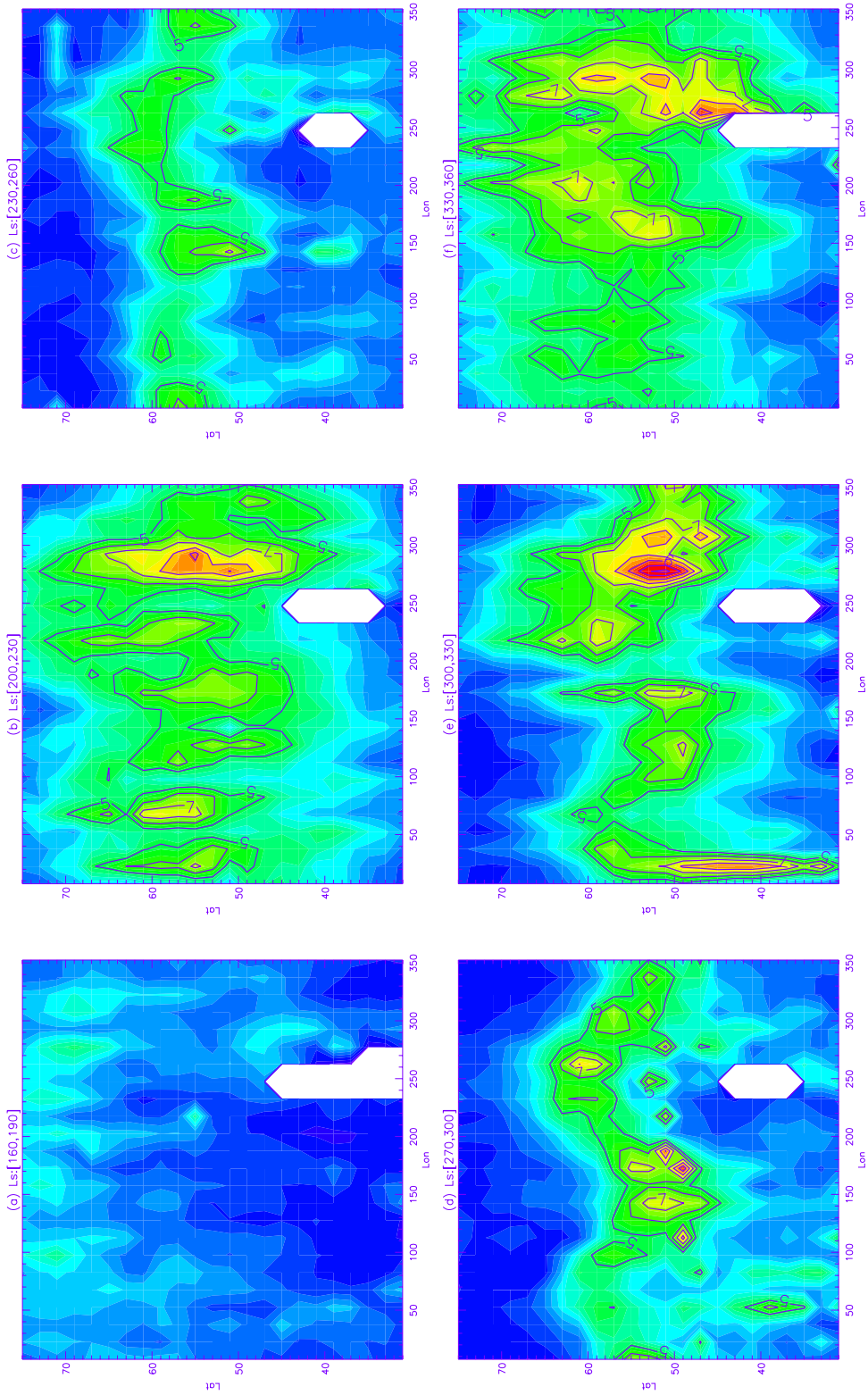

Figure 10. Latitude-(east) longitude distribution of standard deviations of transient temperature perturbations for selected 30° *Ls* periods in MGS mapping Year 1 (1999–2001). The *Ls* periods are (a) 160°–190°, (b) 200°–230°, (c) 230°–260°, (d) 270°–300°, (e) 300°–330°, and (f) 330°–360°. Contours are superimposed on color shadings. Contour interval is 1 K. Every other contour is labeled.

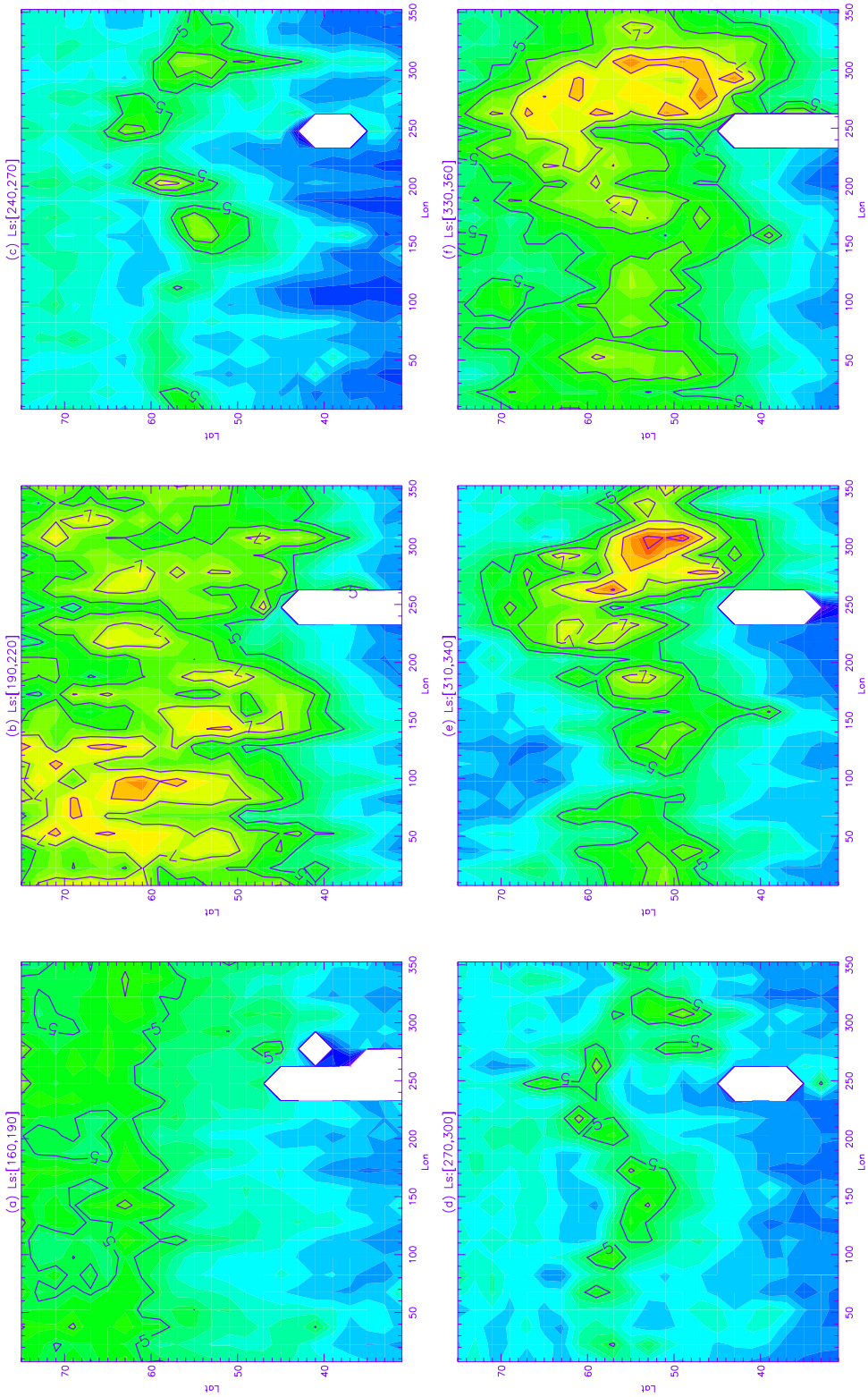

Figure 11. Latitude-(east) longitude distribution of standard deviations of transient temperature perturbations for selected 30° *Ls* periods in MGS mapping Year 3 (2003–2005). The *Ls* periods are (a) 160°–190°, (b) 190°–220°, (c) 240°–270°, (d) 270°–300°, (e) 310°–340°, and (f) 330°–360°. Contours are superimposed on color shadings. Contour interval is 1K. Every other contour is labeled.

activity in the Pacific [*Nakamura*, 1992; *Chang*, 2001]. *Harnik and Chang* [2004] found that the narrowing and strengthening of the jet could explain the decrease of spatial growth rate of baroclinic eddies with shear. Both observations and simulations for the Martian atmosphere show that the north polar jet is generally sharper and stronger during the winter solstice period [*Banfield et al.*, 2003; *Haberle et al.*, 1993]. Although both the Martian storm zones and the terrestrial storm tracks are related to baroclinic instability, there are important differences between them. The terrestrial storm track is characterized as a composite of individual nonlinear baroclinic wave packets with baroclinic energy generation at the entrance, downstream energy transport via downstream development, and barotropic energy dissipation at the exit [*Chang*, 2001]. The midwinter suppression of the Pacific storm track is observed in both the surface pressure and upper-tropospheric velocity and geopotential variance fields [*Chang*, 2001]. The Martian storm zone appears to be linked to flushing dust storms which are associated with small zonal wave number baroclinic eddies. The suppression of transient eddies during the northern winter solstice period is confined to the lower levels in the Martian atmosphere. A detailed quantitative assessment of various factors still requires further study.

4.4. Wave Modes in TES Data

[29] We have used the same space-time decomposition as that of *Banfield et al.* [2004] to identify eastward and westward traveling waves. Figure 12 shows the power of eastward traveling waves with periods of 2–8 sols as a function of latitude and *L*s for MGS Year 1 (MY 24). The top row is for 4.75 mb, and the bottom row for 2.24 mb. The three columns from left to right correspond to zonal wave number m = 1, 2, and 3, respectively.

[30] The top panels of Figure 12 show that m = 3 wave is mainly responsible for the enhanced eddy activity in the lower atmosphere away from the solstice. In fact, the m = 3 waves have periods between 2 and 4 sols [*Banfield et al.*, 2004]. *Banfield et al.* [2004] reported that the m = 3 wave speeded up from a period of 2.8 sols at *L*s $\sim 190^\circ$ to a period of 2.2 sols during *L*s 215°–230°. Successive flushing storms were observed on a daily basis during *L*s 215°–230° in MGS Year 1, and resulted in a planetary-encircling dust storm after *L*s 230°. *Wang et al.* [2003] argued that southward dust transport by baroclinic fronts could be facilitated if dust fronts transverse to Acidalia during the "open tidal gate" hours from 9 AM to 7 PM local solar time when the southward eddy circulation is in phase with the maximum southward component of the diurnal tide circulation. An m = 3 wave with a 2-sol period has a zonal wavelength of 120°, and travels around the pole at $\sim 60^\circ$ longitude/sol. If the first baroclinic fronts associated with the 2.2 sol m = 3 wave happens to be in the low topographic channel during the "open gate" hours, there is a good chance that the next fronts will be a little late in local time but still within the "open gate" hours. This would argue that the 2.2-sol m = 3 wave is more efficient in generating *successive* flushing storms than m = 3 waves with longer periods. The m = 1 and 2 waves at 4.75 mb cover a larger latitudinal range away from the solstice, but the amplitudes show no obvious correlation with the transient temperature standard deviation plot of Figure 8. *Barnes et al.* [1993] presented seasonal changes in baroclinic wave modes simulated by the NASA Ames GCM. Their results show that under clear conditions, the dominant mode at 4 mb is m = 1 at northern winter solstice, m = 2 in early autumn and m = 3 in late winter. Under very dusty conditions, their results show that m = 3 is dominant at 4 mb around the solstice. These GCM results show various similarities and differences with the observations.

[31] The bottom panels (2.24 mb) of Figure 12 show that m = 1 dominates during *L*s 230°–300°, m = 2 dominates in early fall and late winter, and m = 3 is negligible. The shift to smaller zonal wave number at the solstice period is in qualitative agreement with the behavior predicted by simple models such as the Eady model [*Barnes et al.*, 1993]. It is interesting to note that the spatial and temporal distributions of m = 2 on both pressure levels in Figure 12 follow the curves for the polar vortex edge very well (first row of Figure 9), consistent with the wave being associated with the sharp temperature gradient at the polar vortex edge. Figure 12 indicates that m = 3 was relatively close to the surface. *Banfield et al.* [2004] found that m = 2 and 3 were more evident in the fall and spring rather than in the winter solstice period, which was dominated by m = 1. They also found that m = 3 was confined to the lowest scale height. The vertical structure of zonal wave 1 is shown in *Wilson et al.* [2002]. They stated that the simulated waves 2 and 3 are largely confined to below 3 mb. (TES has difficultly showing the low-level structures of these eddies because of the limited vertical resolution and the large longitudinal separation between adjacent orbit tracks). These results suggest that m = 2 or 3 eastward traveling waves in the lower atmosphere are very important for our observed frontal dust storms. m = 1 could interfere with other wave modes to produce sharp traveling fronts (when they have the same phase speed) or storm zones (when they have the same period) [*Banfield et al.*, 2004]. However, m = 1 itself apparently cannot decide the development of frontal dust storms.

5. Summary and Discussion

[32] Long-term observations are invaluable to the study of the Martian atmosphere. The nearly continuous global atmospheric monitoring by MGS has provided us a great opportunity to study the spatial and temporal distribution of different types of clouds and dust storms. This paper summarizes more than two Martian years of observations of frontal dust storms in the northern hemisphere of Mars, and examines the relationship between the morphological features (of dust storms) observed in MOC images and the thermal signatures derived from TES temperatures.

[33] Our results show the existence of cold temperature anomalies behind most dust fronts in the lowest scale height of the atmosphere. Extreme temperature anomalies at 6.1 mb can be as large as −20 K. *Tillman et al.* [1979] presents a detailed study of two front-like events at VL2 (48°N, 226°W) in the fall. One of them is accompanied by a dramatic drop in surface illumination and is interpreted as condensate clouds in the polar hood coming over the landing site [*Tillman et al.*, 1979]. By comparison with our results, the decrease in surface illumination at VL2 can also be caused by substantial amount of dust in baroclinic

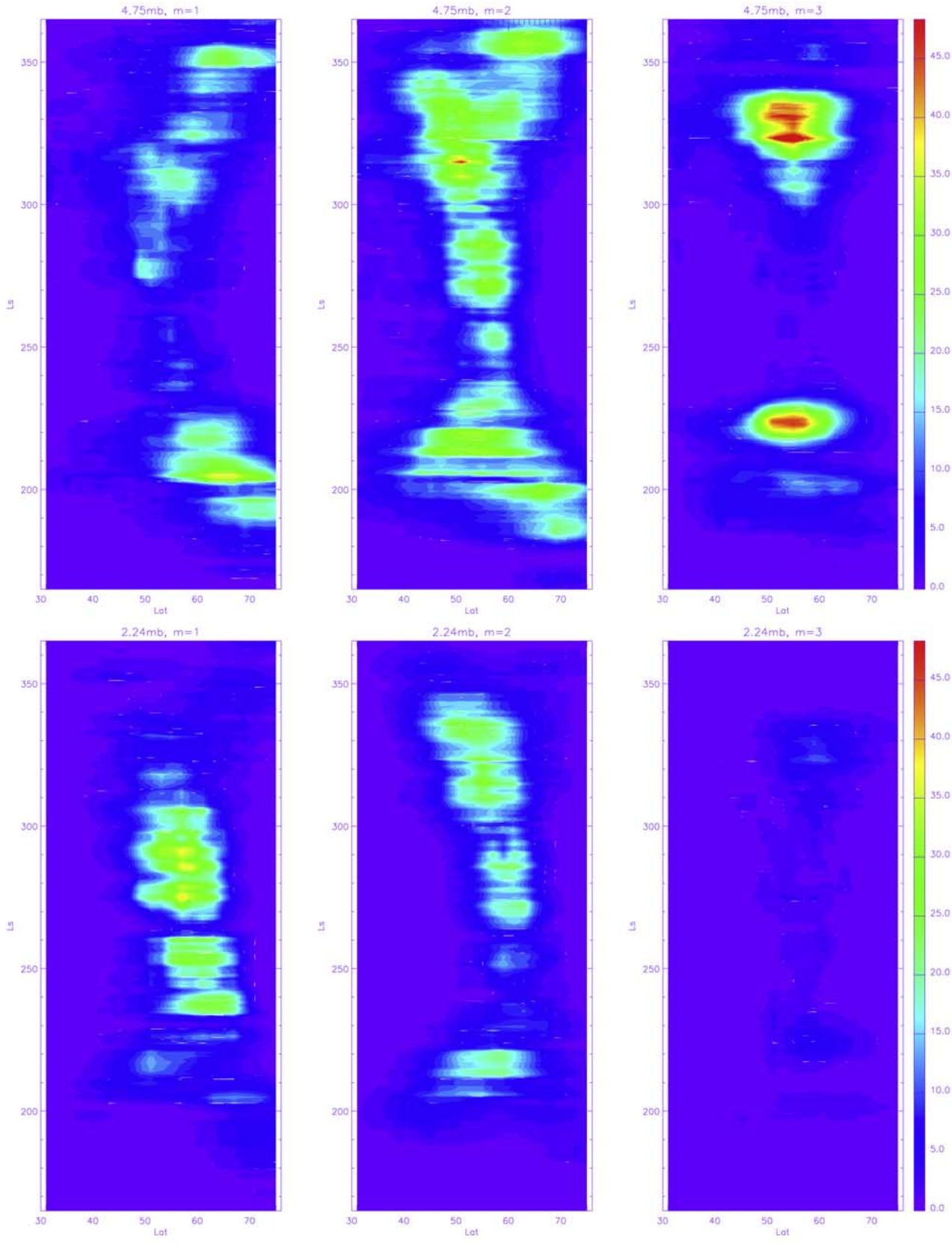

Figure 12. Power (K^2) of eastward traveling waves with periods between 2 and 8 sols for MGS mapping Year 1 (MY 24, 1999–2001). Each panel is a latitude-*Ls* plot. The top row is for 4.75 mb. The bottom row is for 2.24 mb. The three columns from left to right are for zonal wave number m = 1, 2, and 3, respectively.

frontal systems. *Barnes* [1980] found correlations between the VL2 opacities and transient eddy disturbances during early spring of the first Viking year, and preferred the advection of polar clouds as the explanation, but the data were basically consistent with frontal dust storms as well.

[34] The latitudinal and temporal distributions of both frontal dust storms and lower atmosphere transient temperature anomalies show suppressed eddy activity around northern winter solstice for all three MGS mapping years (MY 24–26, 1999–2005). A drop in transient eddy activity around northern winter solstice was also observed by VL2 in the first Viking year (1977–1979) [*Barnes*, 1980]. Analyses of the second Viking year data show that there was a reduction in transient zonal wind variation during L_s 250°–305° though the reduction was not obvious in the perturbation of pressure and meridional wind [*Barnes*, 1981]. It should be cautioned that the VL2 results may be affected by the distance between the lander and the storm zone, in that a poleward shift of the baroclinic zone will lead to a reduction in eddy activity observed by the lander. Some numerical experiments with constant low dust loadings also exhibit minimum eddy activity around northern winter solstice [*Hourdin et al.*, 1995; *Wang et al.*, 2003]. This suggests that there is a purely seasonal effect at work. The atmosphere is drawn closer to the weak eddy regime from the strong eddy regime each year as season progresses from early fall to early winter, and drawn away from the weaker eddy regime as season progresses from early winter to early spring. Large dust storms during the cold season can modulate the timing and amplitude of eddy suppression on top of the seasonal effect. For example, entering the weak eddy regime from the strong eddy regime in the fall may happen sooner in years with large dust storms that happen in the fall. The weak eddy period may be prolonged if a large dust storm occurs near northern winter solstice. A large dust storm that occurs during the strong eddy period in winter may reset the atmosphere to the weak eddy regime, and when the atmosphere comes out of the weak eddy regime, we may expect another period of active eddy activity.

[35] MGS TES data show that, compared to the early-mid fall and mid-late winter periods, the boundary of the polar vortex during the winter solstice period exhibits a cone structure whose walls slope sharply toward the pole with altitude. Such a vortex shape is associated with a sharp temperature gradient and large static stability at the vortex edge. The polar vortex during the winter solstice period is smaller, more circular and stronger. Though the temporal baroclinic eddy growth rate (a theoretical value for unstable waves based on linear theory) attains its maximum near northern winter solstice, the low-level transient eddy temperature amplitudes shows a minimum and no dust storm during this period exhibits classical frontal structure. It is likely that linear growth rates are irrelevant for traveling waves, which are of finite amplitude, and are largely equilibrated. Nevertheless, the data show that the zonal mean structure of the atmosphere during the solstice period is very different from that during the presolstice and postsolstice period, and the nature of the most unstable disturbances change with time substantially. The seasonal variability of traveling wave activity is brought out in *Hourdin et al.* [1995]. *Collins et al.* [1996] discuss the phenomena of zonal wave transitions in model studies. *Leroy et al.* [2003] shows the seasonal variability of simulated waves 1 and 2–3. The latter are most prominent in the Ls 180°–230° period.

[36] The pattern of presolstice fronts–solstice streaks–postsolstice fronts can be understood via the following timescale consideration. The mean time it takes for a parcel to circle the latitudinal circle is $T = L/[u]$, where L is the circumference of the latitudinal circle, [u] is the zonal mean wind speed. The time it takes for eddy turnover is $t^* = \lambda/u^*$, where λ is the wavelength/scale of the eddy, u^* is the eddy wind. Define a parameter $x = t^*/T = (\lambda/L) \cdot ([u]/u^*) = [u]/u^*/m$, where m is the zonal wave number. When $x > 1$, the latitudinal circling time is shorter than the eddy turnover time, streaks tend to form. When $x < 1$, the eddy turnover time is shorter, fronts tend to form. During the northern winter solstice period, [u] is larger, m is smaller. This tends to increase the magnitude of x, consistent with the formation of streaks during the solstice period. It should be noted that the winter solstice period is associated with not only a change of dust storm morphology but also a decrease of dust amount around the north polar night/cap [*Neumann et al.*, 2003; *Smith*, 2004]. Since the polar night area during the solstice period is the largest, it is hard to identify dust events near the terminator in this period and, since the CO_2 ice cap has great southern extent, the regions of the strongest stresses associated with the wave likely lie over frosted surfaces, hence no dust lifting. It simply might be that baroclinic storms really need to get going (develop) at higher latitudes which are well over the cap ice in the heart of winter, but which are much closer to the cap edge in fall and in late winter and spring when most of the frontal dust storms occur. Since the zonal wave number 2 and 3 topographic forcing decreases with latitude in the northern hemisphere, and topography plays key roles in localizing transient eddies, as the polar vortex shrinks toward the pole around northern winter solstice, the topographic effect on the polar circulation may get weaker. This is consistent with the absence of flushing storms during the solstice period.

[37] Simulations show that the strongest meridional velocities are associated with the higher wave numbers, so it is not surprising that dust lifting events are closely related to the m = 3 traveling waves. It is reasonable that topography could modulate the stresses associated with these waves. GCM simulations with parameterized dust lifting (Basu et al., manuscript in preparation, 2005) do, in fact, show that m = 3 traveling waves with ~2-sol period are dominant in initiating the Chryse-type storm that are prominent in their simulations in the Ls 210°–230° period. These waves particularly trigger lifting in the region of Alba Patera, and dust is advected downstream, and, sometimes, into low latitudes through flushing storm events. We suspect that the 2.2 sol m = 3 traveling wave may favor "repeated" flushing dust storms because it tends to keep baroclinic storms within the "open tidal gate hours" for multiple cycles. The Viking Lander 1 (VL1, 22.5°N, 48°W) sits right in the middle of the Acidalia-Chryse flushing dust storm channel. Analyses by *Barnes* [1980] show that vigorous eddy activity is evident at both VL1 and VL2 right up to the start of the 1977b global dust storm. This suggests that flushing dust storms were probably occurring that year. A local dust storm was observed at VL1 during

the clearing of the 1977b great dust storm. Viking orbiter imaging [*James and Evans*, 1981] and Lander data [*Ryan et al.*, 1981] indicated this storm was due to the passage of a baroclinic wave.

[38] **Acknowledgments.** This research project is supported by NASA grant NRA-02-0SS-01. We thank John Wilson for detailed comments on improving the manuscript. We thank Andy Ingersoll for useful discussion. We have benefited from the careful review of the paper by Jeffery Barnes and Don Banfield.

References

Albee, A. L., R. E. Arvidson, F. Palluconi, and T. Thorpe (2001), Overview of the Mars Global Surveyor mission, *J. Geophys. Res.*, *106*(E10), 23,291–23,316.

Banfield, D., B. J. Conrath, M. D. Smith, P. R. Christensen, and R. J. Wilson (2003), Forced waves in the Martian atmosphere from MGS TES nadir data, *Icarus*, *161*, 319–345.

Banfield, D., B. J. Conrath, P. J. Gierasch, R. J. Wilson, and M. D. Smith (2004), Traveling waves in the Martian atmosphere from MGS TES Nadir data, *Icarus*, *170*, 365–403.

Barnes, J. R. (1980), Time spectral analysis of mid-latitude disturbances in the Martian atmosphere, *J. Atmos. Sci.*, *37*, 2002–2015.

Barnes, J. R. (1981), Mid-latitude disturbances in the Martian atmosphere—A 2nd Mars year, *J. Atmos. Sci.*, *38*, 225–234.

Barnes, J. R. (1984), Linear baroclinic instability in the Martian atmosphere, *J. Atmos. Sci.*, *41*, 1536–1550.

Barnes, J. R., J. B. Pollack, R. M. Haberle, B. Leovy, R. W. Zurek, H. Lee, and J. Schaeffer (1993), Mars atmospheric dynamics as simulated by the NASA Ames general circulation model: 2. Transient baroclinic eddies, *J. Geophys. Res.*, *98*(E2), 3125–3148.

Briggs, G. A., and C. B. Leovy (1974), Mariner 9 observations of the Mars north polar hood, *Bull. Am. Meteorol. Soc.*, *55*, 278–296.

Cantor, B. A., P. B. James, M. Caplinger, and M. J. Wolff (2001), Martian dust storms: 1999 Mars Orbiter Camera observations, *J. Geophys. Res.*, *106*(E10), 23,653–23,688.

Chang, E. K. M. (2001), GCM and observational diagnoses of the seasonal and interannual variations of the Pacific storm track during the cool season, *J. Atmos. Sci.*, *58*, 1784–1800.

Christensen, P. R., et al. (2001), Mars Global Surveyor Thermal Emission Spectrometer experiment: Investigation description and surface science results, *J. Geophys. Res.*, *106*(E10), 23,823–23,872.

Collins, M., S. R. Lewis, P. L. Read, and F. Hourdin (1996), Baroclinic wave transitions in the Martian atmosphere, *Icarus*, *120*, 344–357.

Conrath, B. J., J. C. Pearl, M. D. Smith, W. C. Maguire, P. R. Christensen, S. Dason, and M. S. Kaelberer (2000), Mars Global Surveyor Thermal Emission Spectrometer (TES) observations: Atmospheric temperatures during aerobraking and science phasing, *J. Geophys. Res.*, *105*(E4), 9509–9520.

French, R. G., P. J. Gierasch, B. D. Popp, and R. J. Yerdon (1981), Global patterns in cloud forms on Mars, *Icarus*, *45*, 468–493.

Haberle, R. M., J. B. Pollack, J. R. Barnes, R. W. Zurek, C. B. Leovy, J. R. Murphy, H. Lee, and J. Schaeffer (1993), Mars atmospheric dynamics as simulated by the NASA Ames General Circulation Model. 1. The zonal-mean circulation, *J. Geophys. Res.*, *98*(E2), 3093–3123.

Harnik, N., and E. K. M. Chang (2004), The effects of variations in jet width on the growth of baroclinic waves: Implications for midwinter Pacific storm track variability, *J. Atmos. Sci.*, *61*, 23–40.

Hinson, D. P., and R. J. Wilson (2002), Transient eddies in the southern hemisphere of Mars, *Geophys. Res. Lett.*, *29*(7), 1154, doi:10.1029/2001GL014103.

Hinson, D. P., M. D. Smith, and B. J. Conrath (2004), Comparison of atmospheric temperatures obtained through infrared sounding and radio occultation by Mars Global Surveyor, *J. Geophys. Res.*, *109*, E12002, doi:10.1029/2004JE002344.

Hollingsworth, J. L., R. M. Haberle, J. R. Barnes, J. B. Pollack, H. Lee, and J. Schaeffer (1996), Orographic control of storm zones on Mars, *Nature*, *380*, 413–416.

Hollingsworth, J. L., R. M. Haberle, and J. Schaeffer (1997), Seasonal variations of storm zones on Mars, in *Planetary Atmospheres and Ionospheres and Reference Atmospheres*, *Adv. Space Res.*, *19*(8), 1237–1240.

Hourdin, F., F. Forget, and O. Talagrand (1995), The sensitivity of the Martian surface pressure and atmospheric mass budget to various parameters: A comparison between numerical simulations and Viking observations, *J. Geophys. Res.*, *100*(E3), 5501–5524.

James, P. B., and N. Evans (1981), A local dust storm in the Chryse region of Mars, *Geophys. Res. Lett.*, *8*, 903–906.

James, P. B., J. L. Hollingsworth, M. J. Wolff, and S. W. Lee (1999), North polar dust storms in early spring on Mars, *Icarus*, *138*, 64–73.

Kahn, R. (1984), The spatial and seasonal distribution of Martian clouds and some meteorological implications, *J. Geophys. Res.*, *89*, 6671–6688.

Leovy, C. B., and Y. Mintz (1969), Numerical simulation of the atmospheric circulation and climate of Mars, *J. Atmos. Sci.*, *26*, 1167–1190.

Leroy, S. S., Y. L. Yung, M. I. Richardson, and R. J. Wilson (2003), Principal modes of variability of Martian atmospheric surface pressure, *Geophys. Res. Lett.*, *30*(13), 1707, doi:10.1029/2002GL015909.

Lindzen, R. S., and B. J. Farrell (1980), A simple approximate result for the maximum growth rate of baroclinic instabilities, *J. Atmos. Sci.*, *37*, 1648–1654.

Malin, M. C., and K. S. Edgett (2001), Mars Global Surveyor Mars Orbiter Camera: Interplanetary cruise through primary mission, *J. Geophys. Res.*, *106*(E10), 23,429–23,570.

Nakamura, H. (1992), Midwinter suppression of baroclinic wave activity in the Pacific, *J. Atmos. Sci.*, *49*, 1629–1642.

Neumann, G. A., D. E. Smith, and M. T. Zuber (2003), Two Mars years of clouds detected by the Mars Orbiter Laser Altimeter, *J. Geophys. Res.*, *108*(E4), 5023, doi:10.1029/2002JE001849.

Newman, C. E., S. R. Lewis, P. L. Read, and F. Forget (2002), Modeling the Martian dust cycle: 2. Multiannual radiatively active dust transport simulations, *J. Geophys. Res.*, *107*(E12), 5124, doi:10.1029/2002JE001920.

Ryan, J. A., R. D. Sharman, and R. D. Lucich (1981), Local Mars dust storm generation mechanism, *Geophys. Res. Lett.*, *8*, 899–902.

Smith, M. D. (2004), Interannual variability in TES atmospheric observations of Mars during 1999–2003, *Icarus*, *167*, 148–165.

Smith, M. D., B. J. Conrath, J. C. Pearl, and P. R. Christensen (2002), Thermal Emission Spectrometer observations of Martian planet-encircling dust storm 2001A, *Icarus*, *157*, 259–263.

Strausberg, M. J., H. Wang, M. I. Richardson, S. P. Ewald, and A. D. Toigo (2005), Observations of the initiation and evolution of the 2001 Mars global dust storm, *J. Geophys. Res.*, *110*, E02006, doi:10.1029/2004JE002361.

Tillman, J. E., R. M. Henry, and S. L. Hess (1979), Frontal systems during passage of the Martian north polar hood over the Viking Lander 2 site prior to the first 1977 dust storm, *J. Geophys. Res.*, *84*, 2947–2955.

Wang, H., and A. P. Ingersoll (2002), Martian clouds observed by Mars Global Surveyor Mars Orbiter Camera, *J. Geophys. Res.*, *107*(E10), 5078, doi:10.1029/2001JE001815.

Wang, H., M. I. Richardson, R. J. Wilson, A. P. Ingersoll, A. D. Toigo, and R. W. Zurek (2003), Cyclones, tides, and the origin of a cross-equatorial dust storm on Mars, *Geophys. Res. Lett.*, *30*(9), 1488, doi:10.1029/2002GL016828.

Wilson, R. J., D. Banfield, B. J. Conrath, and M. D. Smith (2002), Traveling waves in the Northern Hemisphere of Mars, *Geophys. Res. Lett.*, *29*(14), 1684, doi:10.1029/2002GL014866.

Zurek, R. W., J. R. Barnes, R. M. Haberle, J. B. Pollack, J. E. Tillman, and C. B. Leovy (1992), Dynamics of the atmosphere of Mars, in *Mars*, edited by H. H. Kieffer et al., pp. 835–933, Univ. of Ariz. Press, Tucson.

M. I. Richardson and H. Wang, Division of Geological and Planetary Sciences, California Institute of Technology, MS 150-21, Pasadena, CA 91125, USA. (hqw@gps.caltech.edu)

R. W. Zurek, Jet Propulsion Laboratory, California Institute of Technology, MS 183-335, 4800 Oak Grove Drive, Pasadena, CA 91109, USA.